Unsteady swirling flow in an enclosed cylinder with reflectional symmetry

J. M. Lopez
Department of Mathematics and Earth System Science Center, The Pennsylvania State University, University Park, Pennsylvania 16802

(Received 17 August 1994; accepted 14 July 1995)

A numerical investigation of the multiple stable solutions found in confined swirling flows is presented. The flows consist of fluid in a completely filled cylinder driven by the constant corotation of the two end walls. When reflectional symmetry at the cylinder half-plane is imposed, the flow corresponds to that in a cylinder of half the height driven by the bottom end wall, with the top surface being flat and stress-free. Comparisons with available experiments in this case are made and the observed toroidal recirculation zones attached to the free surface are described in terms of secondary motions induced by the bending of vortex lines. Calculations are also presented where the reflectional symmetry is not imposed and the possibility of the flow breaking this symmetry is discussed. © *1995 American Institute of Physics.*

I. INTRODUCTION

The swirling flow driven in an enclosed cylinder by the constant rotation of one of its end walls gives rise to a rich array of dynamical behavior, including vortex breakdown and the existence of multiple solutions.[1–3] Recently,[4,5] a series of experiments with a variation on the above setup have been conducted. These[4,5] examined the swirling flow in a cylinder driven by the constant rotation of its bottom end wall while the top was a free surface rather than a rigid wall. Hyun[6] has studied this flow numerically; however, the study was restricted to the time-independent equations and covered only a very small part of parameter space. It did not reveal the rich dynamical behavior observed experimentally.[4,5] Daube[7] presented some calculations that match many aspects of the aforementioned experiments. However, the bifurcation structure of the flow was not examined and the onset of time dependence was assumed to be via a supercritical Hopf bifurcation, which the results here show not to be the case.

Spohn *et al.*[5] remark that for the parameter range considered in their experiments, the Froude number was negligibly small. The Froude number gives a relative measure of the extent to which the free surface is deformed by inertial forces such as the centrifugal force due to the swirling motion compared to the restoring gravitational force. Given that the Froude number is essentially zero under the conditions considered, the free surface can be treated as a flat stress-free surface. This flow then corresponds to the situation where the cylinder is twice as long and the flow is driven by the constant corotation of both a top and bottom rigid end wall rotating at the same rate in the same direction and the midplane is a plane of reflectional symmetry (Z_2 symmetry). In the corotating end walls situation, Z_2 symmetry is introduced into the flow, in contrast with the original flows considered by Escudier,[8] Spohn,[4] and Spohn *et al.*,[5] which had no symmetries in the meridional plane. Enforcing the Z_2 symmetry allows one to follow solution branches beyond the point where symmetry breaking would occur. The experiments of Spohn *et al.*[5] essentially do this up to the point where free surface deformations become important. Valentine and Jahnke[9] have also studied this flow numerically for the corotating end walls case, but have concentrated on the steady solutions that retain the Z_2 symmetry; for the most part, they imposed this symmetry and hence did not explore the nature of any symmetry-breaking bifurcations nor the nature of the onset of time dependence.

In the concluding remarks of Spohn *et al.*[5] it is noted that the presence of the free surface leads to very different flow structures compared to when the top is a rigid end wall. It will be demonstrated that the formation of the recirculation zones, referred to as vortex breakdown bubbles, attached to the free surface are a result of the flow responding to axial gradients in the vortex lines, leading to the turning of meridional vorticity into azimuthal vorticity and inducing the reversed meridional circulations, just as in the case when the top is a rigid end wall. The vortex breakdown phenomenon in both the stationary top case and the case with the imposed Z_2 symmetry is qualitatively the same, as is their bifurcation structure. When the Z_2-symmetry condition is relaxed, the bifurcation structure of the corotating case may be richer due to the breaking of Z_2 symmetry. We find that the Z_2 symmetry is broken only in the time-dependent solutions, and then, only on "coarse" grids. All steady solutions without Z_2 symmetry imposed were found to be Z_2 symmetric.

II. GOVERNING EQUATIONS AND THEIR NUMERICAL SOLUTION

The equations governing the flow are the axisymmetric Navier–Stokes equations, together with the continuity equation and appropriate boundary and initial conditions. It is convenient to write these using a cylindrical polar coordinate system (r,ϑ,z), with the origin at the center of the bottom rotating end wall and the positive z axial direction being toward the top. Since the flow is axisymmetric, there exists a Stokes streamfunction ψ and the velocity vector in cylindrical polars is

$$\mathbf{u}=\left(-\frac{1}{r}\psi_z, v, \frac{1}{r}\psi_r\right). \tag{1}$$

Subscripts denote partial differentiation with respect to the subscript variable. This form of the velocity automatically satisfies the continuity equation. It is also convenient to in-

 1070-6631/95/7(11)/2700/15/$6.00

troduce a new variable, the angular momentum $\Gamma = rv$. Here Γ is proportional to the circulation. The vorticity field corresponding to (1) is

$$\boldsymbol{\omega} = (\xi, \eta, \zeta) = \left(-\frac{1}{r}\Gamma_z,\ -\frac{1}{r}\nabla_*^2\psi,\ \frac{1}{r}\Gamma_r \right),$$

where

$$\nabla_*^2 = (\ )_{zz} + (\ )_{rr} - \frac{1}{r}(\ )_r.$$

The velocity and vorticity fields can be decomposed into azimuthal (ϑ) and meridional (m) fields, where

$$\mathbf{u}^{\vartheta} = \left(0, \frac{1}{r}\Gamma, 0 \right),$$

$$\boldsymbol{\omega}^{\vartheta} = \left(0, -\frac{1}{r}\nabla_*^2\psi, 0 \right),$$

$$\mathbf{u}^{m} = \left(-\frac{1}{r}\psi_z, 0, \frac{1}{r}\psi_r \right),$$

and

$$\boldsymbol{\omega}^{m} = \left(-\frac{1}{r}\Gamma_z, 0, \frac{1}{r}\Gamma_r \right);$$

so $\boldsymbol{\omega}^{\vartheta} = \nabla \times \mathbf{u}^{m}$ and $\boldsymbol{\omega}^{m} = \nabla \times \mathbf{u}^{\vartheta}$. Further, Γ plays the role of a streamfunction for the meridional vorticity field.[10] In other words, contours of Γ in a meridional plane are cross sections of vortex surfaces (vortex lines), just as contours of ψ are cross sections of streamsurfaces (streamlines). These give the local direction of the vorticity and velocity vectors in the plane, respectively, and the azimuthal components of the vectors give the degree to which the vectors are directed out of the plane. If the flow were inviscid and steady, Γ would be a function of ψ alone.

The axisymmetric Navier–Stokes equations, in terms of ψ, Γ, and η, are

$$D\Gamma = \nabla_*^2\Gamma/\mathrm{Re}, \tag{2}$$

$$D\left(\frac{\eta}{r}\right) = \left[\nabla^2\left(\frac{\eta}{r}\right) + \frac{2}{r}\left(\frac{\eta}{r}\right)_r \right] \Big/ \mathrm{Re} + \left(\frac{\Gamma^2}{r^4}\right)_z, \tag{3}$$

where

$$\nabla_*^2\psi = -r\eta,$$

$$D = (\ )_t - \frac{1}{r}\psi_z(\ )_r + \frac{1}{r}\psi_r(\ )_z, \tag{4}$$

$$\nabla^2 = (\ )_{zz} + (\ )_{rr} + \frac{1}{r}(\ )_r,$$

and $\mathrm{Re} = \Omega R^2/\nu$. The length scale is the radius of the cylinder R, the time scale is $1/\Omega$, Ω is the constant angular speed of the rotating end wall, ν is the kinematic viscosity, and the other governing nondimensional parameter is the cylinder aspect ratio H/R; H being the cylinder height in the case of a stationary rigid end wall, or, in the corotating end walls case, it is the distance from an end wall to the midplane of the cylinder.

Equation (3) shows that inertial change in the azimuthal vorticity, and hence a source of the overturning meridional flow, is driven by axial gradients in the angular momentum. The physical origin[11] of the source term on the right-hand side of (3) is the azimuthal component of $\nabla \times (\mathbf{u}^{\vartheta} \times \boldsymbol{\omega}^{m})$. It corresponds to the turning of meridional vorticity into the azimuthal direction by the azimuthal velocity. Brown and Lopez[2] found the necessary condition, in the limit of steady, inviscid flow, such that the turning of the meridional vorticity produces azimuthal vorticity of the correct sign so as to locally induce a reversal in the direction of the meridional flow. The condition for this flow reversal to be possible is that the ratio of the tangents of the helix angles of the velocity and vorticity vectors be greater than unity on streamsurfaces upstream of the reversal in the meridional flow.

A. Computational technique

Details of the computational technique, together with accuracy and resolution tests, are given in Lopez[1] for the stationary top end wall case. In summary, the governing equations are discretized on a uniform finite-difference grid using second-order central differences to approximate all spatial derivatives except those in the advection terms, which are approximated using the second-order conservative scheme of Arakawa.[12] No artificial viscosity is used; instead, a sufficiently fine grid is used to ensure proper resolution of spatial scales and grid-independent solutions. For the steady solution branch with Re up to approximately 3000 and $H/R = 1.5$, this is achieved on a uniform grid consisting of $nr = 61$ nodes in the radial and $nz = 91$ nodes in the axial directions. The steady computations of Valentine and Jahnke[9] were performed on uniform grids using second-order central differences for Re up to 3000, and they report that there were no significant differences between the results using grid sizes of 1/60 and 1/120. Further grid refinement tests and the use of a stretched grid are detailed in the following section for higher Re flows than those considered in Lopez,[1] including time-dependent solutions, and for the corotating end walls case.

Time integration uses the explicit alternating time-step scheme of Miller and Pearce.[13] For $1000 < \mathrm{Re} < 4000$, stability of the scheme is primarily governed by the Courant–Friedrichs–Levy condition, and this is amply satisfied by a time step $\delta t = 0.05$ on the 61×91 grid. For $\mathrm{Re} < 1000$, the diffusion requirement,[14]

$$\delta t < \delta r^2\ \mathrm{Re}/8,$$

dominates the stability of the scheme, where δr is the spatial resolution (all results presented have $\delta r = \delta z$).

A number of different types of initial conditions have been employed in this study. The first consists of an impulsive start from rest, where initially all cylinder walls and the fluid are at rest. At $t = 0$, one end wall or both end walls (depending on the particular case being studied) are set to rotate at a constant angular speed Ω. A second type of initial condition consists of taking a steady solution at some Re as the initial condition for a calculation with a different value of Re. This second initiation was used to continue the steady branch to large Re, using small increments in Re so as not to start the calculations outside the basin of attraction of the

steady solution branch. A steady state is determined to have been reached when the relative change between ψ, η, and Γ at time step k and at time step $k+1$, at all grid points, is less than 10^{-6}. Another initial condition, albeit nonphysical, consists of a fully developed flow in the bottom half (the flow with Z_2 symmetry imposed at the same or nearby parameter values) and setting everything to zero in the top half of the cylinder. This initial condition is used to determine the robustness of the Z_2 symmetry.

The boundary conditions on the free surface are $\eta=0$, $\Gamma_z=0$, and $\psi=0$; on the axis of symmetry, $\eta=0$, $\Gamma=0$, and $\psi=0$; on stationary rigid walls, $\eta=-\psi_{nn}/r$, $\Gamma=0$, and $\psi=0$; and on rotating rigid end walls, $\eta=-\psi_{nn}/r$, $\Gamma=r^2$, and $\psi=0$. The subscript n denotes differentiation normal to the wall. One-sided differences from a Taylor-series expansion to second-order centered about one grid point in from the boundary are used to discretize derivative boundary conditions. Use is also made of the fact that normal derivatives of ψ on rigid walls are zero. The discrete version of the vorticity boundary conditions are $\eta(1,j)=0$; $\eta(nr,j)=-2\psi(nr-1,j)/\delta r^2$; $\eta(i,1)=-2\psi(i,2)/[r(i)\delta z^2]$; $\eta(i,nz)=-2\psi(i,nz-1)/[r(i)\delta z^2]$ (stationary rigid top); $\eta(i,nz)=0$ (corotating end walls with imposed Z_2 symmetry); and $\eta(i,2nz-1)=-2\psi(i,2nz-2)/[r(i)\delta z^2]$ (corotating end walls without imposed Z_2 symmetry).

B. Grid resolution study

Of great concern to this study is the question of sufficient grid resolution. This is particularly important, as the discretized set of governing equations constitute a finite-dimensional dynamical system whose bifurcation structure (singular points of the dynamical system) can differ significantly from those of the continuous equations (the infinite-dimensional dynamical system). There are numerous examples in the literature demonstrating this. Particular examples are that of solutal convection[15] and flow past a sphere in a pipe,[16] where the existence of spurious Hopf bifurcations as a result of insufficient grid resolution have been revealed.

In regions of parameter space where only a unique steady solution exists in the continuous system, beyond a certain level of resolution in the discrete system, the corresponding solution (termed the "low" resolution solution) does not change qualitatively as the level of grid resolution is increased, and the solution changes quantitatively in an asymptotic manner, converging to the solution of the continuous system. There are formal theoretical results for the Galerkin discretization of the Navier–Stokes equations, which suggest generalizations to other discretizations. Constantin, Foias, and Temam[17] have shown that if the computed approximations of the time-dependent equations "seem to converge" to some limit as $t\to\infty$, then the same is true for the exact problem and the two limits are related.

However, in regions of parameter space where multiple solutions exist, formal results concerning convergence of the discrete system appear to be lacking. This situation is far more complicated. In the previous situation, the phase space of the system had only one attractor (the unique steady solution). Now there is more than one attractor and hence one needs to consider not only whether the attractors are converging to those of the exact problem, but also if their basins of attraction are converging. Even if the level of resolution is such that the attractors of the discrete system are asymptotically similar to those of the exact problem, their basins of attraction may not have converged at that level of resolution, and hence conclusions about the stability of the attractors of the continuous system based on the stability of the attractors of the discrete system may not be correct. Also, for similar initial conditions, evolution on systems of different resolution may not end up on the "same" attractor, because the structure of the basins of attraction may be such that the initial condition at one level of resolution is in the basin of attraction of a different attractor to that at another level of resolution. Determining the structure of the basin of attraction for the Navier–Stokes equations is a nontrivial exercise. Consider how complicated it can be for relatively simple equations (the Julia set and the Mandelbrot set).

Here, we determine the level of grid resolution required, within a region of parameter space, for the discretized equations to give consistent (i.e., not changing with further grid resolution) qualitative behavior (the solutions may continue to change quantitatively in an asymptotic manner). We do this in a number of ways. First, in a region of parameter space where only a single steady state exists, we determine the level of grid resolution required for the solution to be quantitatively in the asymptotic region. We monitor the maximum and minimum values of ψ and η on the grid points, both on a uniform grid and a stretched grid. Next, using a time-dependent code, we take the steady solutions with different levels of resolution and use continuation to follow the steady branch to higher Re. By increasing the grid resolution and reducing the increments in the continuation parameter (typically Re), the level of grid resolution for consistent qualitative behavior is determined.

The stretched grid is given by

$$r=x-a\,\sin(2\pi x)$$

and

$$z=[y-b\,\sin(2\pi y)]H/R,$$

where $x=i/(nr-1)$, for $i=0\to(nr-1)$; $y=j/(nz-1)$, for $j=0\to(nz-1)$; and in all the results presented here, the stretching factors $a=b=0.1$ have been used. This stretching places the grid points more densely near the boundaries, the axis, and the midplane when Z_2 symmetry is imposed. When employing the stretched grid, second-order central differences are used to discretize the equations spatially. We begin by determining a suitable level of resolution at a large Re $=2600$, where the only solution is steady (see Sec. IV for this determination). Table I gives the extreme values of ψ and η for the case Re$=2600$, $H/R=1.5$, both on the uniform and the stretched grids of various sizes, together with the δt used. The δt's are approximately the smallest on a given grid for which the system was stable. This information, together with the visual information provided by the plots of the solutions in Fig. 1, indicates that the 61×91 uniform grid solution is in the asymptotic range of the continuous solution. Given that δt on a uniform grid with about the *same* number of grid

TABLE I. Minimum and maximum values of ψ and η on the grid points of the various grids, as indicated, for Re=2600 and $H/R=1.5$ at steady state.

Grid	δt	min(ψ)	max(ψ)	min(η)	max(η)
31×46 uniform	1.0×10^{-1}	-7.741×10^{-3}	2.860×10^{-4}	−6.522	11.08
61×91 uniform	5.0×10^{-2}	-7.709×10^{-3}	3.777×10^{-4}	−4.496	17.58
121×181 uniform	2.5×10^{-2}	-7.608×10^{-3}	3.747×10^{-4}	−4.222	20.62
241×361 uniform	7.5×10^{-3}	-7.555×10^{-3}	3.714×10^{-4}	−4.217	21.42
51×76 stretched	1.0×10^{-2}	-7.539×10^{-3}	4.234×10^{-4}	−4.196	20.94
101×151 stretched	5.0×10^{-3}	-7.537×10^{-3}	3.832×10^{-4}	−4.213	21.49
151×226 stretched	2.5×10^{-3}	-7.532×10^{-3}	3.756×10^{-4}	−4.215	21.60

points as on a stretched grid is larger, the 61×91 uniform grid is preferred because it is sufficiently accurate, essentially grid independent, and efficient, at least for the steady solution branch up to Re≈3×10^3.

Testing the grid independence of the solutions in regions of parameter space where multiple solutions exist is more complicated. For Re>2600 (and $H/R=1.5$), we have found that using grids with less resolution than the uniform 61×91 grid, the steady solution branch loses stability at Re≈2650 (the exact value of Re depends on the grid resolution). However, for grids with at least the resolution of the uniform 61×91 grid, the steady solution branch remains stable up to Re=3200. These results are detailed in Sec. III. We have confirmed this by recalculating a part of the steady branch on the 101×151 stretched grid using $\delta t=0.005$ (the uniform 61×91 grid used $\delta t=0.05$). The steady solutions were continued from the unique steady solution at Re=2600. Using δRe=50, the steady Re=2650 was reached after approximately 1000 time units. Figure 2 gives the time series of $\psi(nr=51,\ nz=76)$ for the continuation runs. The transient oscillations in the Re=2650 calculation, initiated with the Re=2600 steady solution, begin to grow, but are soon highly damped as the flow adjusts to the sudden increase in Re. Physically, this corresponds to an impulsive increase of ≈2% in the rotation rate of the disk, Ω. If a larger δRe is used, the initial transients are not damped and the flow evolves to the periodic solution branch. If the same δRe is used, starting from the Re=2650 steady solution, the flow evolves to the periodic branch. However, a smaller δRe=25 results in a steady Re=2675 solution, and from that solution to the Re =2700 solution. To continue beyond Re=2700, a δRe=10 had to be employed. All the transients, up to Re=2790, using this δRe, are damped; as illustrated in Fig. 2. Using δRe =10 at Re=2790 to continue the branch to Re=2800 was not successful and the flow evolved to the periodic branch. A detail of the corresponding time series is presented in Fig. 3.

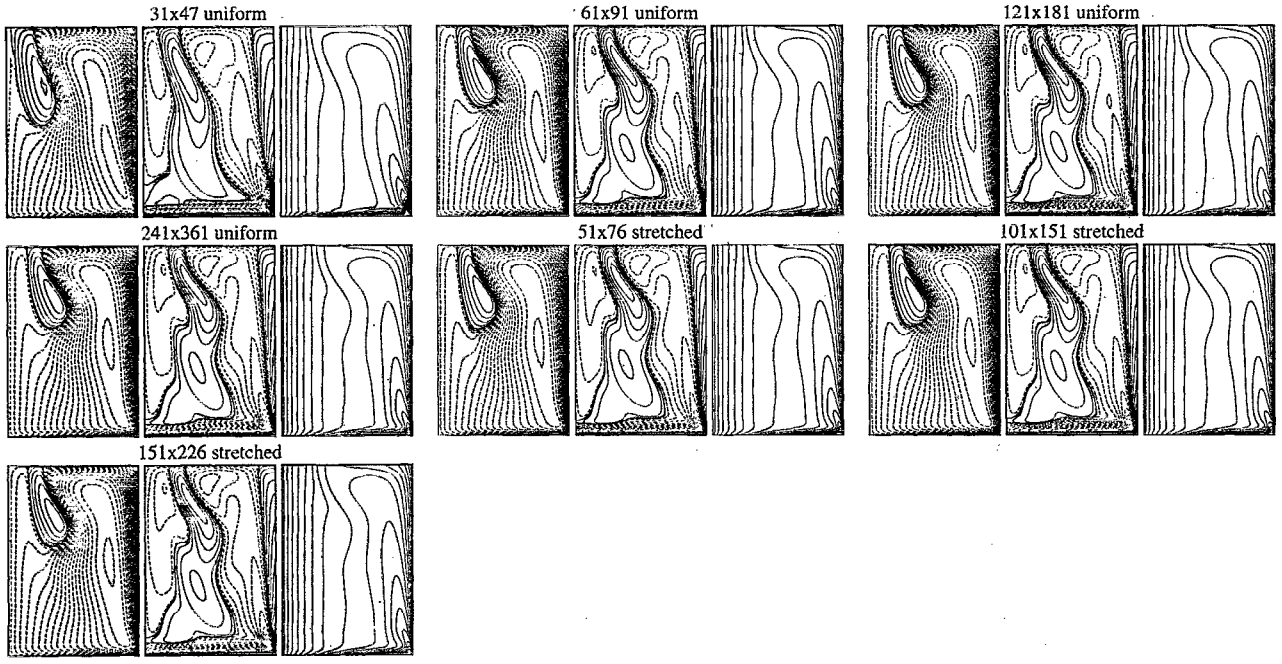

FIG. 1. Steady Z_2-symmetric flows (only the bottom half of the cylinder is shown) for Re=2600 and $H/R=1.5$ calculated on various grids: (a) 31×47, uniform, $\delta t=0.1$; (b) 61×91, uniform, $\delta t=0.05$; (c) 121×181, uniform, $\delta t=0.025$; (d) 241×361, uniform, $\delta t=0.0075$; (e) 51×76, stretched, $\delta t=0.01$; (f) 101×151, stretched, $\delta t=0.005$; (g) 151×226, stretched, $\delta t=0.0025$. The contour levels for (i) ψ, (ii) η, and (iii) Γ are nonuniformly spaced, with 20 positive (solid lines) and 20 negative (dashed lines), determined by the c level(i)=Max(variable)×$(i/20)^3$ and c level(i) =Min(variable)×$(i/20)^3$, respectively, with $i=1\rightarrow20$. For all plots the following have been used: Max(ψ)=10^{-3}, Min(ψ)=-10^{-2}, Max(η)=20, Min(η)=−6, Max(Γ)=1, and Min(Γ)=0.

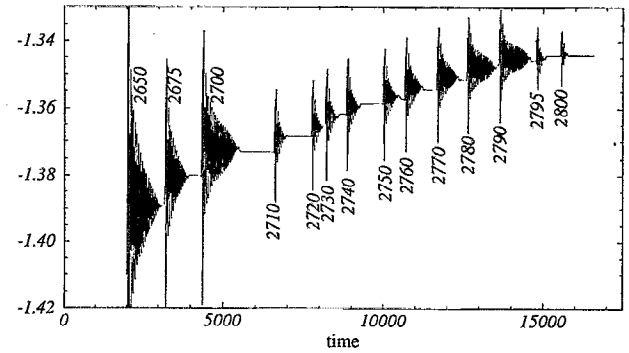

FIG. 2. Time series of $10^3\psi(nr=51, nz=76)$ for the continuation run on the 101×151 stretched grid using $\delta t=0.005$, started from the steady Re=2600 solution. The values of Re following each impulsive, incremental increase are noted on the plot.

Continuing this calculation for a further 2000 time units results in the periodic solution detailed in Fig. 4 (discussed in Sec. IV). A calculation such as this is suggestive of a supercritical Hopf bifurcation. However, if instead of using δRe =10 we use δRe=5 from the steady Re=2790 solution, the steady Re=2800 solution is reached, as illustrated in Fig. 2. There is no supercritical Hopf bifurcation here, merely the existence of two *stable* solution branches, one of them steady and the other time periodic, and which one is realized depends on the initial conditions. Figure 5 gives the steady solutions at Re=2790, 2795, and 2800. Note that the three solutions are virtually indistinguishable, yet the Re=2790 solution is to "far away" (i.e., outside the basin of attraction) from the Re=2800 solution, yet the Re=2795 solution is not, illustrating how sensitive the stable solutions on the steady branch are. Compare the solution for Re=2800 in Fig. 5, on the stretched 101×151 grid with that in Fig. 6(j), on the uniform 61×91 grid; they are in very close agreement. The qualitative behavior of the steady branch is the same on both the 61×91 uniform grid and the higher resolution 101×151 stretched grid.

The grid resolution study provides confidence in the accuracy of the determined stability of the steady branch, and also that the time-dependent branch is disjoint from the steady branch, or at least it does not originate via a supercritical Hopf bifurcation from it (see Sec. IV).

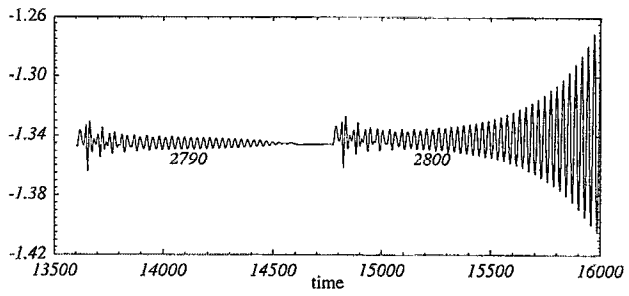

FIG. 3. Details of the time series of $10^3\psi(nr=51, nz=76)$ for the continuation run on the 101×151 stretched grid using $\delta t=0.005$, started from the steady Re=2780 solution, using δRe=10, leading to a periodic solution for Re=2800.

III. PRODUCTION OF SECONDARY FLOW BY VORTEX LINE BENDING

The flows under consideration are a part of a larger class of confined flows driven by angular momentum gradients. The primary motion is due to externally imposed rotation imparting a vertical (i.e., parallel to the rotation axis) component of vorticity to the flow. The particular details of the enclosing geometry imposes kinematic constraints on the flow resulting in the bending of vortex lines. The bending of vortex lines produces secondary motions, primarily associated with the azimuthal component of vorticity. In a large class of these flows, the secondary motions can be comparable to the primary motion, leading to significant nonlinear interactions. One such interaction manifests itself as recirculation bubbles in the interior of the flow, and is often referred to as vortex breakdown. The particular details of the topology of these recirculation zones depends on the details of the geometry of the container and the strength of the driving force, yet they all result from the bending of vortex lines. A great deal is made of the differing details of the streamsurfaces of these recirculation zones, with suggestions that these differences may reflect different processes at work. However, the topology of the streamsurfaces is not a particularly useful diagnostic for uncovering the dynamical processes at play. More suited is a study of the vortex lines (or vortex surfaces) and how the geometry of the container bends these, producing the rich array of secondary motions.

A. Vortex line structure of the flows

For the confined flow driven by the bottom rotating end wall with a flat stress-free top surface, the primary flow is due to the rotating end wall. The vortex lines all emanate from this end wall, as the fluid in contact must move with it. The sidewall of the cylinder, being stationary, is a vortex surface corresponding to $\Gamma=0$ and the axis of symmetry, $r=0$, is also a vortex line corresponding to $\Gamma=0$. The vortex lines emanating from the rotating end wall correspond to a $\Gamma(r,0)=r^2$ distribution. Hence, the corner where the rotating end wall and the stationary sidewall meet is singular, with Γ varying from 1 on the end wall to 0 on the sidewall. Vortex lines may terminate at this corner. For the case where the top is rigid and stationary, all the vortex lines emanating from the rotating end wall must terminate at this corner. However, when the top is a flat stress-free surface, or equivalently, at the midplane when Z_2 symmetry is imposed in the corotating end walls case, the vortex lines have the option of meeting the surface (midplane) orthogonally. This option is responsible for the secondary motions being different to those of the stationary rigid top case. Also, the vortex lines meeting the midplane divide the flow into an inner and an outer region. The inner region is $r \leqslant r_\Gamma(z)$, where $r_\Gamma(z)$ is the location of the vortex line emanating from the rotating end walls (but not from the corners) with largest radius, which meets the midplane. The two regions are particularly distinct at larger Re and their interface supports waves (see Sec. IV).

As in the case of a rigid top, the bending of the vortex lines in the limit of creeping flow is due solely to the kinematic constraints of the container. The vortex line bending

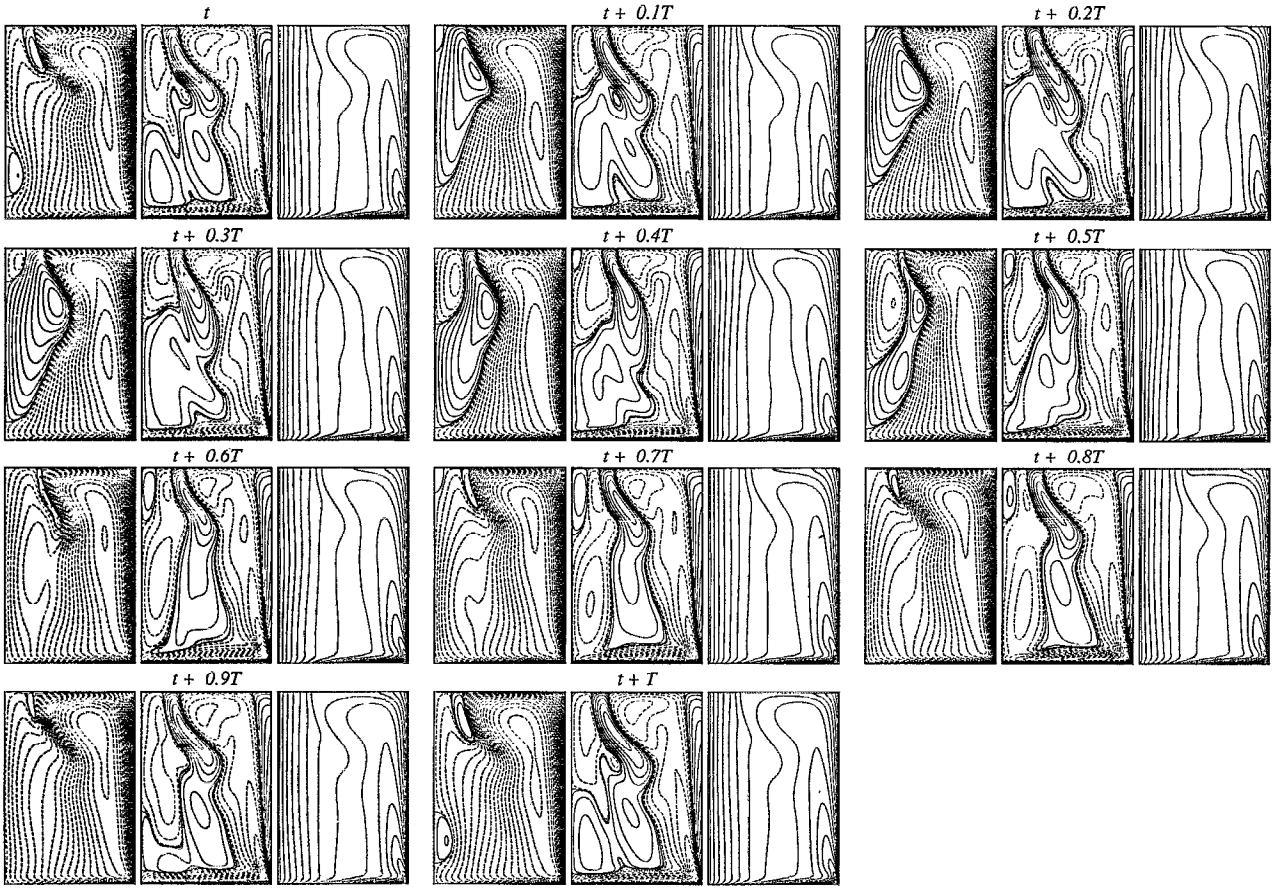

FIG. 4. Eleven equally spaced phases over one period ($T \approx 28.2$) of the periodic Z_2-symmetric solution for Re=2800 and $H/R=1.5$, and its time average, calculated on the 101×151 stretched grid with $\delta t=0.005$. The contours are as determined in Fig. 1.

leads to axial gradients in Γ and via the term $(\Gamma^2/r^4)_z$ in Eq. (3), azimuthal vorticity is produced, inducing the secondary meridional flow. This secondary meridional flow is responsible for the establishment of the Ekman layer on the rotating end wall and at larger Re, advects high Γ fluid from the Ekman layer into the interior. In so doing, the secondary meridional flow sweeps the vortex lines near the Ekman layer radially outward. This nonlinear interaction between the primary flow (vertical vorticity) and the secondary flow (azimuthal vorticity) causes further bending of the vortex lines and an enhancement of the meridional flow transporting further fluid with high Γ into the interior. This process near the rotating end wall is essentially independent of the form of the top, at least qualitatively, for small Re. Hyun[6] also made this observation. However, how the high Γ fluid behaves near the top does depend on whether it is a rigid or a flat stress-free surface, as conditions there on Γ are different. The conditions on η are also different, but $\psi=0$ on the top regardless of whether it is stress-free or rigid. The condition $\psi=0$ at the midplane does not necessarily apply in the corotating end wall case if Z_2 symmetry is not imposed.

B. Flow development for increasing Re

At low Re ($\lesssim 1$), the flow is essentially at the limit of Stokes (creeping) flow. At this limit, the flow has all the symmetries of the container, i.e., azimuthal symmetry, and in the corotating end walls case, both the flow and the container have Z_2 symmetry. The results of Serrin[18] ensure that in the limit of low Re, the flow is unique and steady. The primary

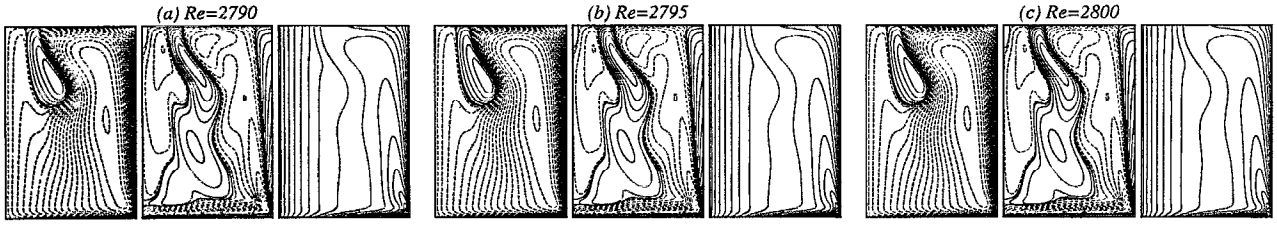

FIG. 5. Steady Z_2-symmetric solutions for $H/R=1.5$ and (a) Re=2790, (b) Re=2795, and (c) Re=2800; calculated on the 101×151 stretched grid with $\delta t=0.005$. The contours are as determined in Fig. 1.

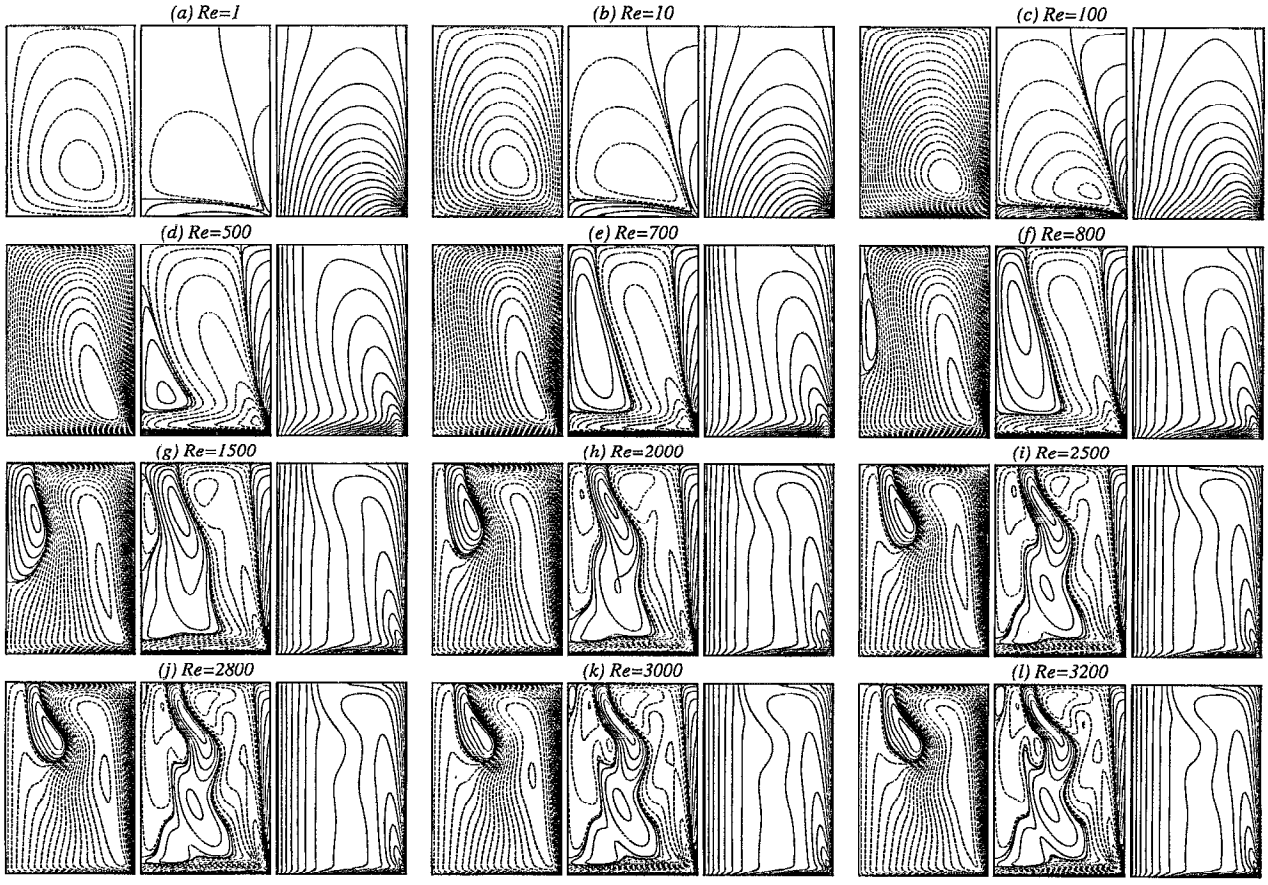

FIG. 6. Steady Z_2-symmetric solutions for Re as indicated and $H/R=1.5$, calculated on the 61×91 uniform grid with $\delta t=0.05$. The contours are as determined in Fig. 1.

flow consists of meridional vortex lines, which in the absence of rigid stationary end walls and sidewall, would remain parallel to the rotation axis. However, as discussed in Sec. III A, the kinematic constraints of the container lead to the bending of the vortex lines and the establishment of a secondary meridional circulation. Figure 6(a) is a plot of the steady flow for Re=1 and $H/R=1.5$ on the bottom half of the cylinder, the top boundary is the Z_2 symmetry plane. The discussion of the flow development as Re varies is restricted to the case of $H/R=1.5$ for the sake of brevity.

The majority of the vortex lines emanating from the rotating end walls, in the Stokes flow limit, are bent and terminate at the corner ($r=1$, $z=0$). Only the vortex lines corresponding to $\Gamma \ll 1$ meet the symmetry plane. This bending results in a negative (positive) axial gradient in Γ, turning the meridional vorticity into the negative (positive) azimuthal direction in the bottom (top) half of the cylinder, and hence induces meridional circulations. These secondary circulations consist of radial outflow at the rotating end walls, flow

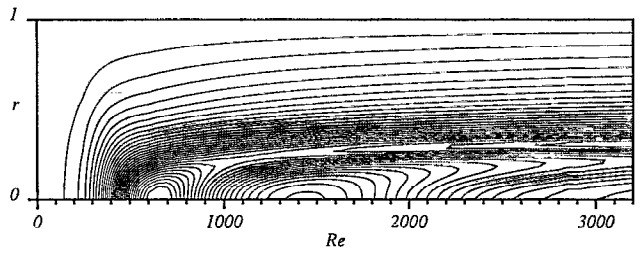

FIG. 7. Contours of v/r (determined from the steady Z_2-symmetric solutions calculated on a 61×91 uniform grid with $\delta t=0.05$) at the Z_2-symmetry plane versus Re. The contours are uniformly spaced and the increment between them is 1/40. At $r=1$, $v/r=0$; v/r is a maximum at $r=0$ and Re ≈650. From that maximum, there extends a maximum ridge line toward larger Re with $r\approx 0.25$. There is also a local minimum in v/r at $r=0$ and Re≈1450.

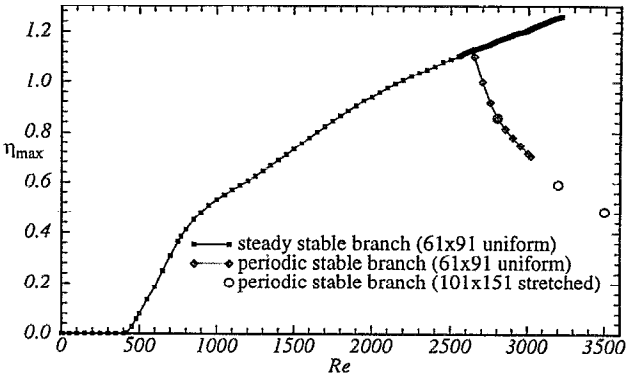

FIG. 8. State diagram using η_{max} as the state variable, for $H/R=1.5$. This diagram was primarily determined from the 61×91 uniform grid solutions and "spot-checked" using the 101×151 stretched grid solutions.

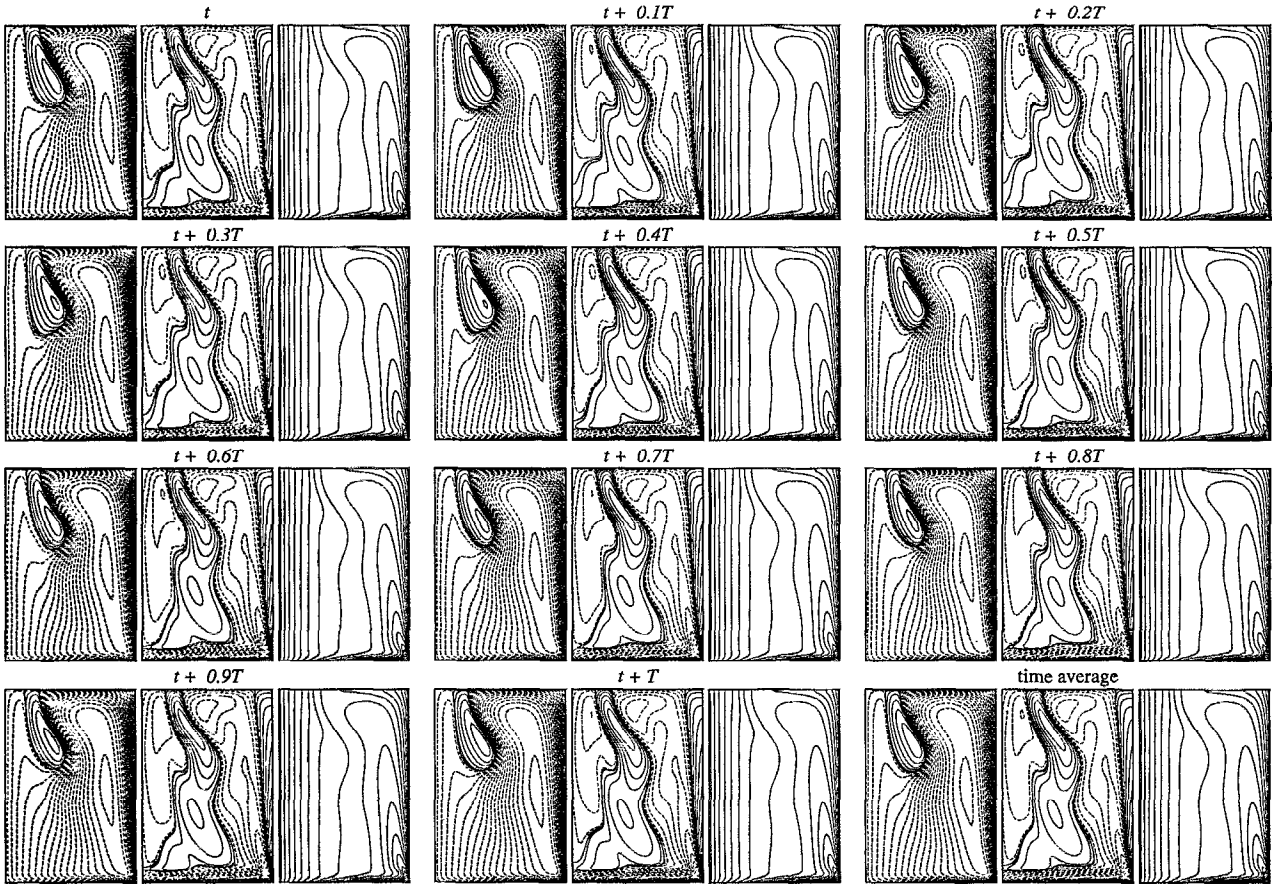

FIG. 9. Eleven equally spaced phases over one period ($T\approx28.5$) of the periodic Z_2-symmetric solution for Re=2640 and $H/R=1.5$, and its time average calculated on the 61×91 uniform grid with $\delta t=0.05$. The contours are as determined in Fig. 1.

toward the symmetry plane along the stationary sidewall, radial inflow at the symmetry plane, and a return to the rotating end walls along the axis. In the Stokes flow limit, the magnitude of these secondary circulations scales with Re. Figure 6(a) shows the flow at Re=10 in the bottom half of the cylinder. Here, Γ remains essentially unchanged and ψ and η have been scaled by Re, in comparison with the Re=1 case. By Re=100, the secondary circulation is strong enough to advect the Γ vortex lines with it. This is quite evident in Fig. 6(c) just above the Ekman layer on the rotating end wall. This local advection of the Γ vortex lines by the secondary circulation is strong enough by Re=500 to locally produce positive (negative) axial gradients in Γ, turning meridional vorticity into the positive (negative) azimuthal direction [Fig. 6(d)]. At Re=500, this locally produced positive (negative) η via the nonlinear interaction between the primary (Γ) and secondary (ψ) flow is quite weak. However, by Re=700 [Fig. 6(e)], the positive (negative) η is large enough to induce a local undulation in the streamlines. In accord with the experimental observations of Spohn *et al.*[5] by Re=800, the positive (negative) η is large enough that the meridional flow on the axis stagnates and a recirculation zone results [Fig. 6(f)].

The faster meridional flow bends the Γ vortex lines in the Ekman layer region as more angular momentum is carried with the flow. This enhances the negative (positive) axial gradients in Γ, resulting in more negative (positive) η, and reenforces the secondary meridional circulation.

The faster meridional flow also carries angular momentum acquired in the Ekman layer farther up (down) the sidewall with increasing Re, and results in vortex lines corresponding to increasingly larger values of Γ, meeting the

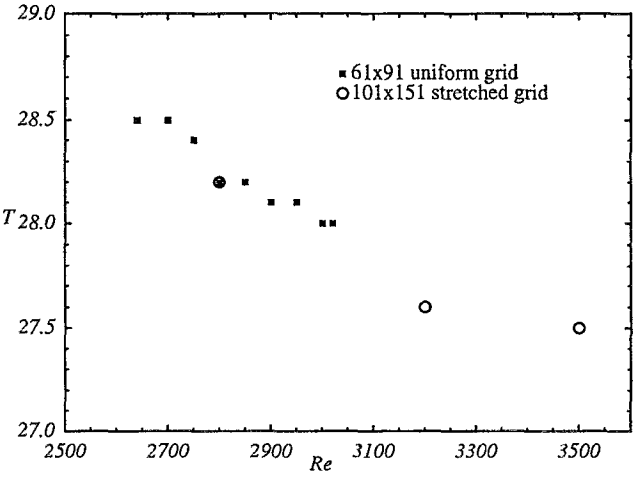

FIG. 10. Variation of the period of oscillation, T, with Re on the $T\approx28$ periodic solution branch.

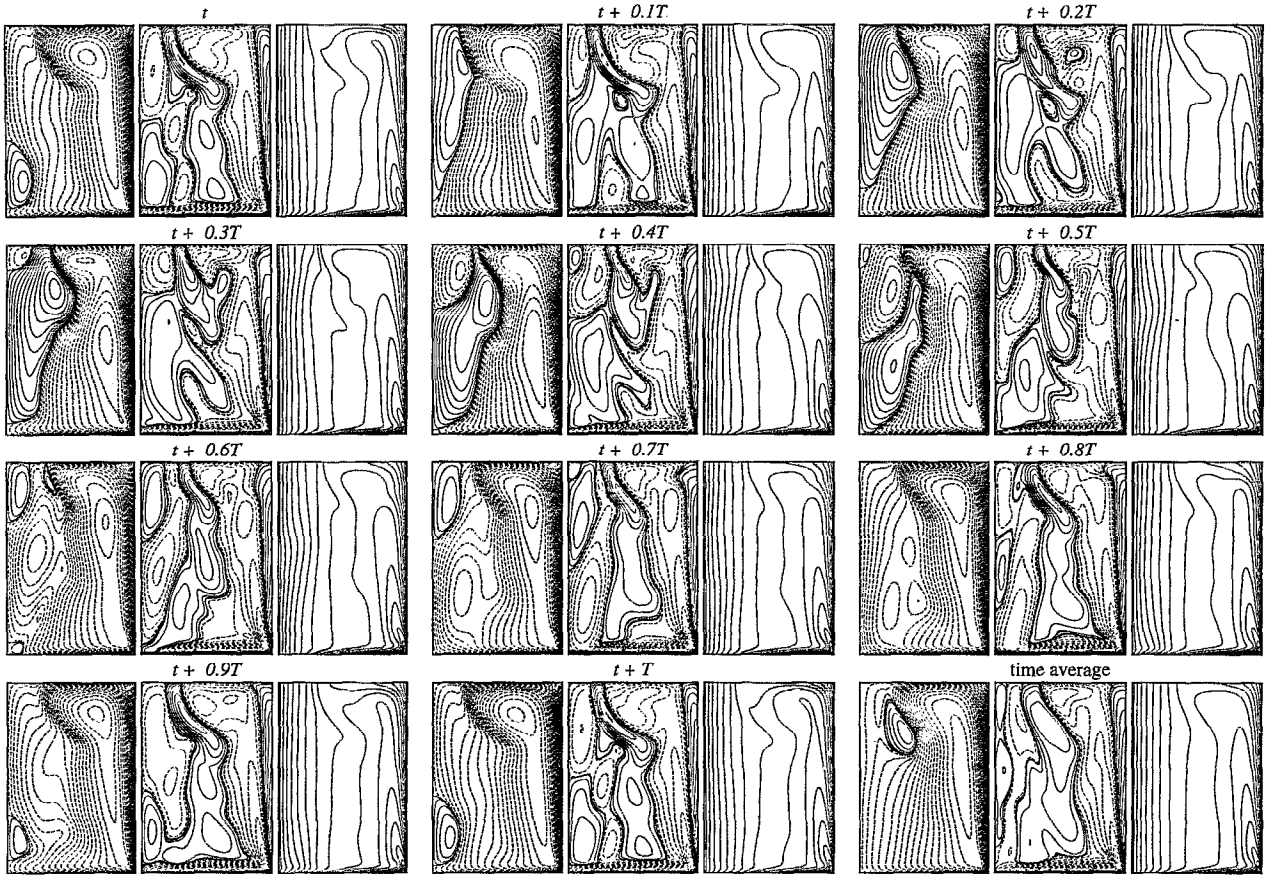

FIG. 11. Eleven equally spaced phases over one period ($T \approx 27.5$) of the periodic Z_2-symmetric solution for Re=3500 and $H/R=1.5$, and its time average, calculated on the 101×151 stretched grid with $\delta t=0.005$. The contours are as determined in Fig. 1.

symmetry plane orthogonally. This in effect produces a radial jet of high Γ fluid being injected into the interior at the symmetry plane.

Spohn *et al.*,[5] based on inviscid arguments, suggest that the radial jet of high Γ fluid injects angular momentum in toward small radii only up to the point where the angular velocity of the fluid, v/r, increases to match the angular velocity of the rotating disk, Ω, which is equal to 1 in nondimensional units. At about this point (it will vary slightly due to viscous effects) the meridional flow no longer continues to flow radially inward, but instead stagnates on the free surface and turns into the axial direction, thereby forming the observed toroidal recirculation zone attached to the free surface. For low Re flow, the viscous effects near the free surface (even though there is no rigid wall, there are still axial gradients in the velocity contributing to viscous stresses near the free surface) are sufficient for the flow to dissipate enough angular momentum as it flows radially inward so that v/r on the free surface remains sufficiently less than 1 and no separation is required. This experimentally observed behavior is also observed in our calculations of the corotating case with Z_2 symmetry imposed, where the symmetry plane corresponds to the free surface in the experiments.

Figure 7 shows the development of v/r on the symmetry plane for increasing Re along the steady solution branch. At low Re, v/r is negligibly small on the symmetry plane. With increasing Re, v/r increases monotonically from zero with decreasing r. At Re$\approx$680, v/r has a local maximum of $\approx$0.82 at $r=0$. It is at about this Re that η near the symmetry plane changes sign [cf. Figs. 6(d) and 6(e)]. At this Re, the meridional flow has not stagnated on the symmetry plane, but as Re increases, the radius at which v/r attains its maximum value of $\approx$0.8 moves farther out from the axis and the region of positive (negative) η intensifies. By Re=800 [Fig. 6(f)], the locally increased $|\eta|$ is large enough to induce a reversed meridional flow halting the inward meridional flow provided by the Ekman pumping on the rotating end walls. This results in stagnation on the symmetry plane and the formation of a recirculation zone, termed a vortex breakdown by Spohn *et al.*[5] Certainly, the reversed meridional flow here is induced by the azimuthal vorticity η resulting from the bending of the vortex lines, just as are the recirculation zones on the axis in both the corotating end walls case and the stationary rigid top case. The radius at which v/r is a maximum corresponds more closely with the radius at which η changes sign near the symmetry plane than with the radius at which the meridional flow stagnates. For Re>700, v/r decreases toward $r=0$, and there is a local minimum in v/r at $r=0$ for Re$\approx$1450. From Fig. 6(g), corresponding to Re=1500, η changes sign again very near $r=0$. For Re >1500, v/r has a maximum at $r\approx0.25$ and a local minimum at $r\approx0.15$. The maximum corresponds to the change in sign

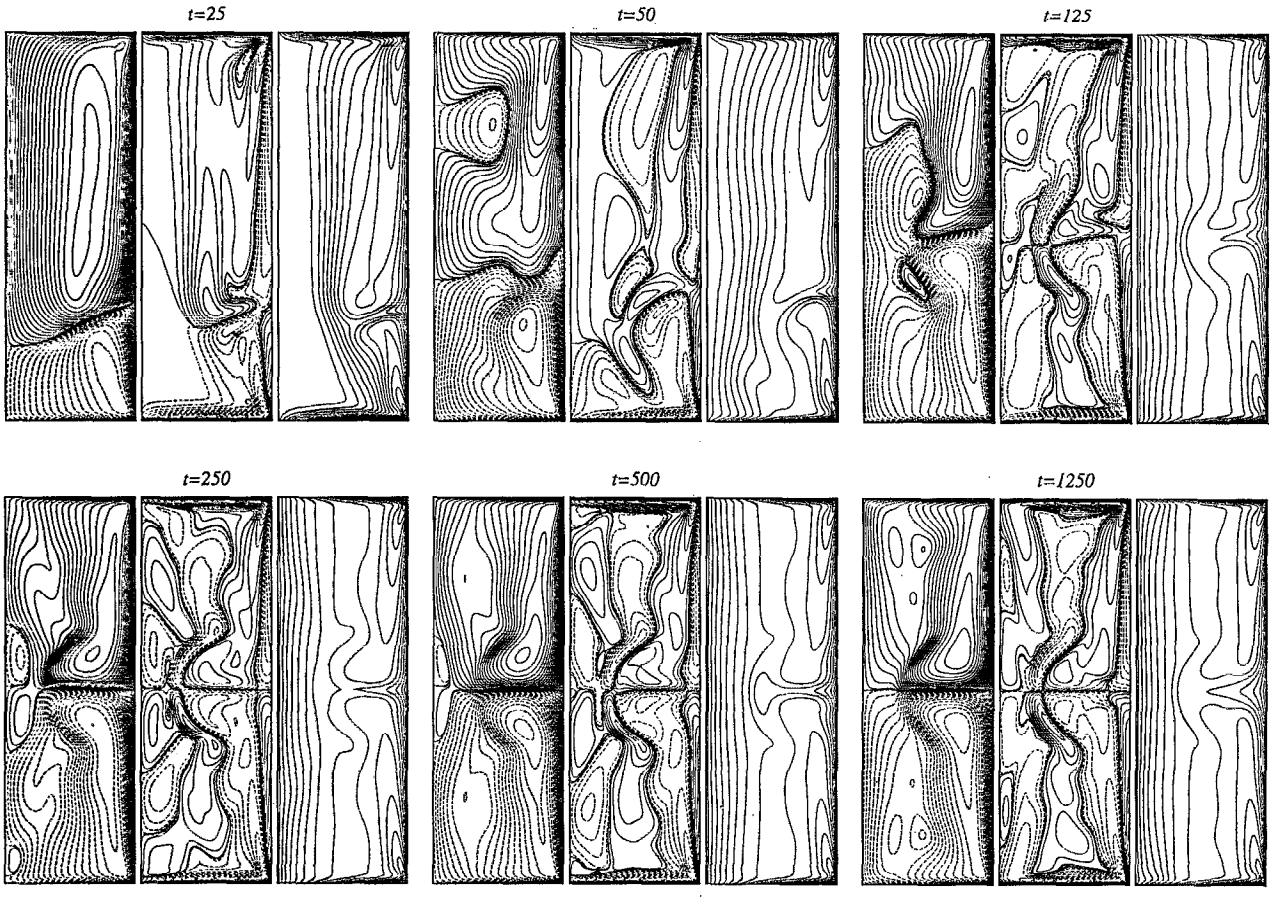

FIG. 12. Evolution for Re=3500, $H/R=1.5$, calculated on the 101×301 stretched grid, with $\delta t=0.005$, and Z_2 symmetry not imposed. The evolution was started at $t=0$ from the asymmetric initial condition described in Sec. II A; times as indicated. The contours are as determined in Fig. 1; except that here $\mathrm{Max}(\psi)=10^{-2}$ and $\mathrm{Min}(\eta)=-20$.

of η as r decreases and the minimum corresponds to a second change in the sign of η as r decreases further. For increasing Re, the inner region of negative (positive) η induces radial inflow. By Re=2000 [Fig. 6(h)], this induced radial inflow is large enough to reattach the separated flow onto the symmetry plane, forming the toroidal recirculation zone. Figure 6(h) is in very close agreement with the flow visualization of Spohn *et al.*[5] in their Fig. 5(a), corresponding to Re =2095, $H/R=1.5$.

Figure 8 is a state (bifurcation) diagram for the corotating end walls flow. The bifurcation parameter is Re (a fixed $H=1.5$ is employed) and the quantitative measure of the flow state is $\eta_{\max}$, the maximum positive value of η in the interior of the bottom half of the cylinder. For periodic flows (Sec. IV), $\eta_{\max}$ is the maximum positive value of η of the time-averaged flow in the interior of the bottom half of the cylinder. The interior is defined as being the region in from the boundaries delineated by the first zero contour of η (note that $\eta\geqslant0$ on and near the rigid boundaries in the bottom half and $\leqslant0$ in the top half of the cylinder; see Fig. 6). Any quantitative measure of the flow state can be used, and $\eta_{\max}$, a local measure, is not necessarily optimal. However, the qualitative picture of the state diagram is unaffected by the choice and $\eta_{\max}$ is convenient and illustrates some of the flow physics.

IV. ONSET OF UNSTEADY Z_2-SYMMETRIC FLOW

The steady solution branch (Fig. 8) described in the preceding section remains stable to time-dependent and Z_2-symmetry breaking disturbances (at least for Re$\leqslant$3200). As in the case of the rigid stationary top, a disjoint periodic branch has been found. For $H/R=1.5$, it originates as a turning point bifurcation at Re$\approx$2640 (at Re=2630, only a steady solution is found to exist; whereas, at Re=2640, both a periodic and a steady solution exist). In order for the time-periodic branch to originate as a subcritical Hopf bifurcation from the steady branch, the steady branch would have to be unstable beyond the Re corresponding to the subcritical Hopf bifurcation, but we find the steady solution to be stable at least for Re$\leqslant$3200. The basin of attraction of the steady branch becomes increasingly small for increasing Re and a continuation in Re for Re$\approx$3200 requires increments, δRe, of the order of 0.01% in order to guarantee that the initial conditions remain within the basin of attraction of the steady solution. For Re$\approx$2650, increments of the order of 2% are small enough. Some further discussion of the dependence of the basin of attraction on the grid resolution is provided in Sec. II B. Such a small basin of attraction gives the impression that the onset of time dependence is via a supercritical Hopf bifurcation (Daube[7] assumes this to be the case, but

does not explore other possibilities). This impression is caused if the initial conditions are placed outside the basin of attraction of the steady branch, or if an imposed disturbance (physically, this could be due to a slight wobble in the rotating end walls, a nonconstant rotation rate Ω, or temperature fluctuations) perturbs the flow out of the basin. The resulting evolution to a time-periodic state only shows that the steady solution is unstable to *finite-amplitude* disturbances, but does not allow conclusions concerning its *linear* stability. Valentine and Jahnke[9] conclude that their steady solution at Re $=3000$, $H/R=1.5$, is unstable to *finite-amplitude* disturbances, the disturbances being the differences between the central difference used to discretize the steady equations to get their steady solution and the upwind differencing used in their time-dependent code. They did not attempt to do time-dependent calculations with more carefully selected initial conditions. Calculations with carefully selected initial conditions placed within the basin of attraction of the steady solution branch, such as those reported here, clearly show the steady solutions to be stable and to coexist with the periodic solutions. Hence, a supercritical Hopf bifurcation from the steady branch cannot be the origin of the periodic solution branch. Otherwise, the steady branch would have to be *linearly* unstable beyond the supercritical Hopf bifurcation point, and a time-dependent calculation using the steady solution as an initial condition, together with a perturbation of *any* size (even as small as numerical roundoff), would evolve away from the steady solution. As detailed in Sec. II B, on a sufficiently refined grid, this does not happen.

The attractiveness (i.e., larger, in some sense, basin of attraction) of the periodic solution over the steady solution can be understood as follows. For axisymmetric steady flows in the limit as Re$\rightarrow\infty$, the streamlines (ψ) and the vortex lines (Γ) must coincide. However, at the symmetry plane (or flat stress-free surface) they must be orthogonal. At low Re, viscosity acts to adjust the flow, but as Re increases, the flow must either lose its axial symmetry or become unsteady in order that the streamlines and vortex lines need not coincide. The experiments of Spohn *et al.*[5] suggest that the flow first becomes unsteady rather than nonaxisymmetric as Re is increased.

In the periodic flow, the radial jet of high Γ flow at the midplane overshoots the mark at which $v/r\approx 1$, and recoils, overcorrecting, then overshoots again and so on. At Re $=2640$ (see Fig. 9), this results in a weak periodic wobbling, in the radial direction, of the toroidal recirculation bubble. The oscillation is highly damped in the axial direction. As Re is increased, this behavior is further enhanced. By Re$=2800$, each wobble sends a pulse in the axial direction along the interface between the inner flow (i.e., the region near the axis where the vortex lines originating on the end walls meet the symmetry plane orthogonally) and the outer flow. This pulse

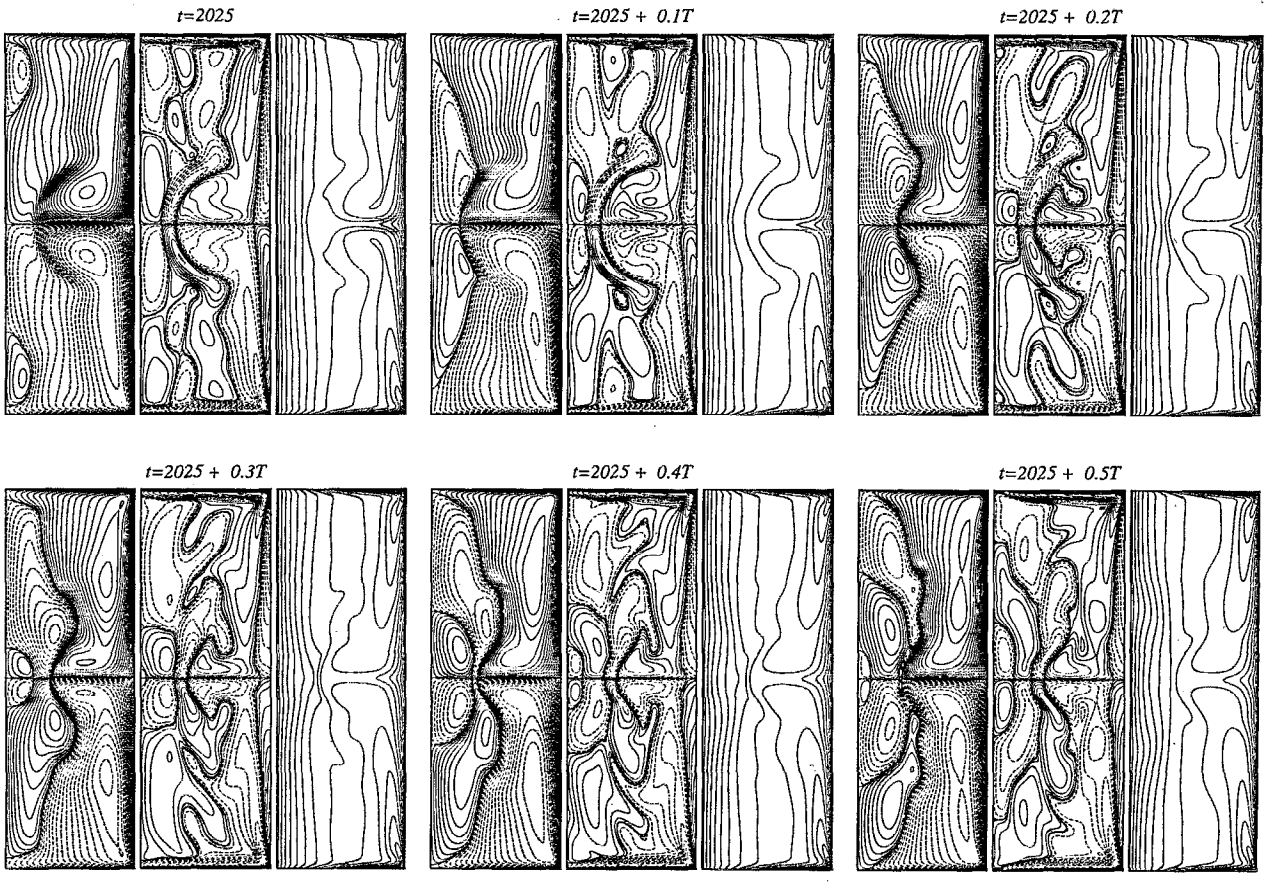

FIG. 13. Eleven equally spaced phases over one period ($T\approx 27.5$) of the flow depicted in Fig. 12, times as indicated, and its time average. The contours are as determined in Fig. 12.

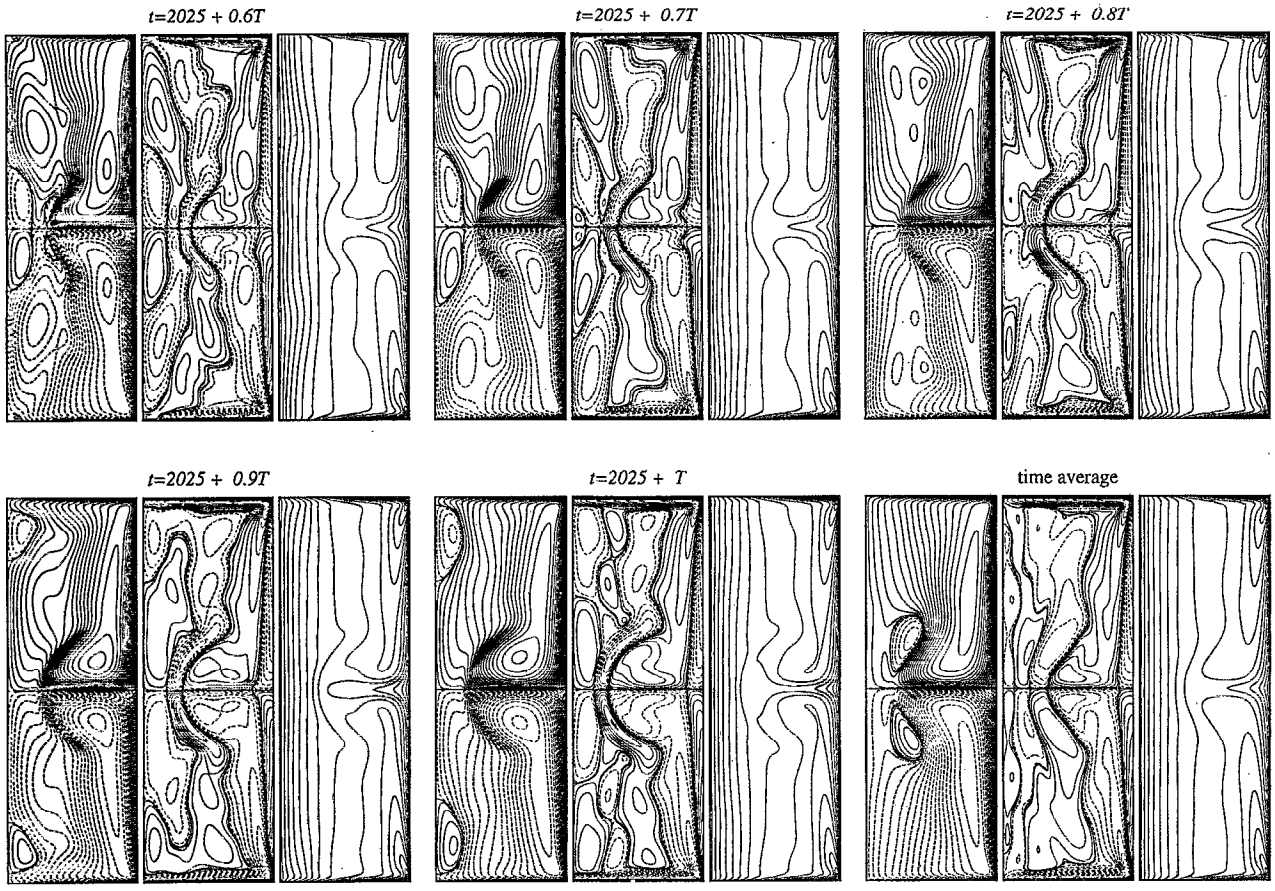

FIG. 13. (*Continued.*)

just reaches the rotating end wall and is reflected back along the axis. At this Re, the reflected pulse is highly damped by viscous effects, and is just discernible in Fig. 4.

Unlike the rigid top end wall case, where the frequency of oscillation for a particular aspect ratio is independent of Re over a large range,[3,7] the frequency of the flat stress-free surface case does show a slight variation with Re. This was also noted by Daube[7] in his calculations. Figure 10 shows the variation of the period of oscillation, T (nondimensionalized by Ω), with Re for the Z_2-symmetric flow with $H/R=1.5$ impulsively started from rest. The periodic flow is first observed at Re=2640 with a period $T\approx 28.5$, and, at Re=2800, the period has decreased to $T\approx 28.2$. Figure 10 is constructed using both the 61×91 uniform grid and the 101×151 stretched grid. The period at Re=2800 was determined on both grids and agreed to three figures. At Re=3030, there is period doubling to a flow with $T\approx 56.0$, when calculated on the 61×91 uniform grid. At Re=3050, also on the 61×91 uniform grid, the flow evolves from rest to the period $T\approx 28$ flow and eventually changes to one with $T\approx 18.75$. As Re is further increased, using the same grid, the period increases in contrast to the trend at lower Re, and at Re=3350 a further

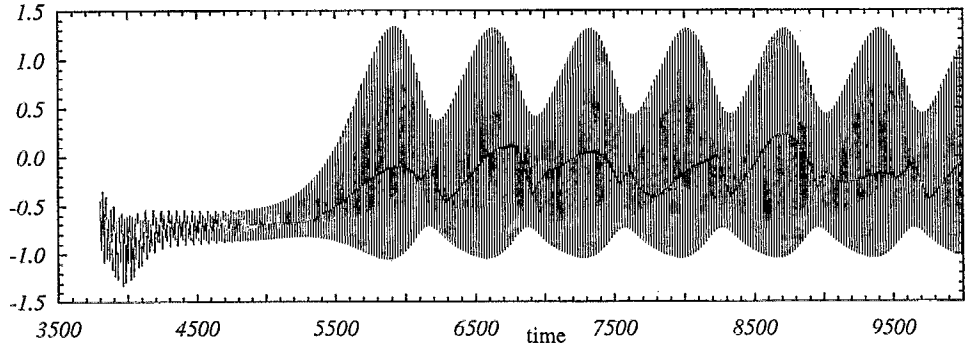

FIG. 14. Time series of $10^3\psi$ ($nr=51$, $nz=150$) for Re=3200, $H/R=1.5$ calculated on the 101×301 stretched grid using $\delta t=0.005$, started at $t=3750$ from the asymmetric initial condition described in Sec. II A.

period doubling is observed. However, if these higher Re cases are computed on the 101×151 stretched grid, the aforementioned higher-frequency modes and the period doublings are not observed. Calculations started from rest on the stretched grid at Re=2800, 3200, and 3500 all evolved to the single-frequency periodic flow on the $T\approx 28$ branch, the only time-dependent branch found with the 101×151 stretched grid (see Figs. 8 and 10) when Z_2 symmetry is imposed and the calculations are impulsively started from rest. This strongly suggests that the higher-frequency modes and the period doublings are numerical artifacts, due to insufficient resolution. Figure 11 shows the Re=3500 flow over one period ($T\approx 27.5$). The overshooting of the high Γ radial jet at the symmetry plane causing a pulse to travel along the interface between the inner and outer regions to the rotating end walls, and then its reflection along the axis, as described earlier for Re=2800 (Fig. 4) is more enhanced at this higher Re.

V. Z_2-SYMMETRY BREAKING

So far, only the Z_2-symmetric flow has been considered. The experimental flow[4,5] with a free surface is the physical analog of this flow, up to the point where free surface deformations are no longer negligible. In this section, we consider the possible breaking of the Z_2 symmetry (note that this is not related to free surface deformations). Azimuthal symmetry continues to be imposed, and the breaking of this symmetry remains an open question.

Impulsively started calculations from an initial state of rest without imposed Z_2 symmetry reach the same steady state as when the symmetry is imposed for Re≤2600 on both the 61×91 uniform and the 101×151 stretched grids (when Z_2 symmetry is not imposed, the grid has $nr\times[2(nz-1)+1]$ grid points, i.e., 61×181 and 101×301 on the uniform and stretched grids, respectively). For 2640≤Re≤2800, the same Z_2-symmetric periodic flow was achieved as when symmetry was imposed, using either grid. These Z_2-symmetric solutions are reached even when very nonsymmetric initial conditions are used (the third initial condition described in Sec. II A). For Re≤2600, these initial conditions evolve to the steady Z_2-symmetric solution branch. For 2640≤Re≤2800, these initial conditions evolve to the Z_2-symmetric periodic branch. However, on the 61×91 uniform grid, for 2850≤Re≤3000, a Z_2-symmetric periodic flow was reached, but its period ($T\approx 18.6$) was different to that of the flow when Z_2 symmetry was explicitly imposed ($T\approx 28.2$). The initial condition consisted of the $T\approx 28.2$ flow in the lower half and zero flow in the top half. It is curious that $18.6\times 1.5=28.2$, remembering that here $H/R=1.5$.

Here Z_2-symmetry breaking on the 61×91 uniform grid

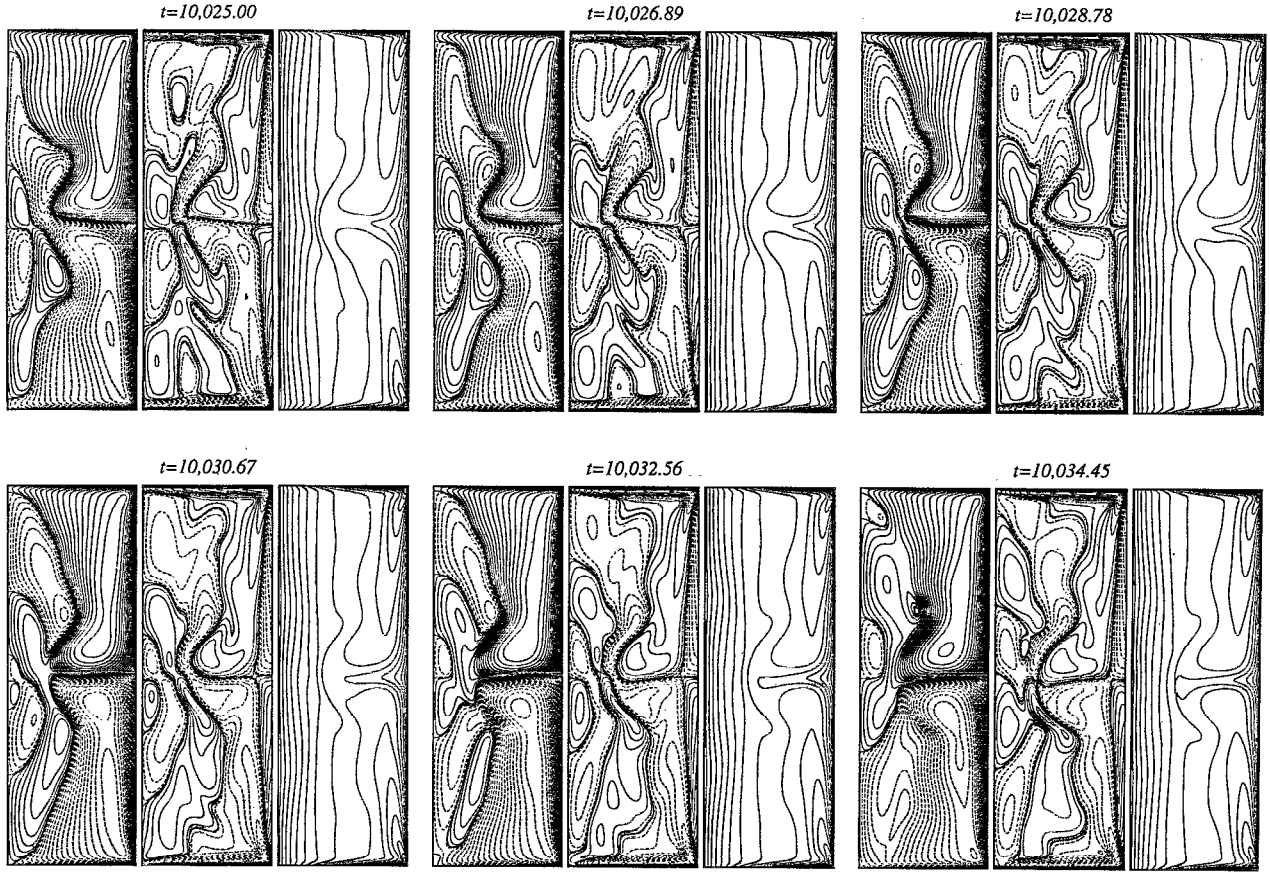

FIG. 15. Eleven equally spaced solutions, at times as indicated, and their average over that time period, of the modulated periodic flow with Z_2 symmetry not imposed for Re=3200, $H/R=1.5$ calculated on the 101×301 stretched grid using $\delta t=0.005$, started at $t=3750$ from the asymmetric initial condition described in Sec. II A. The contours are as determined in Fig. 12.

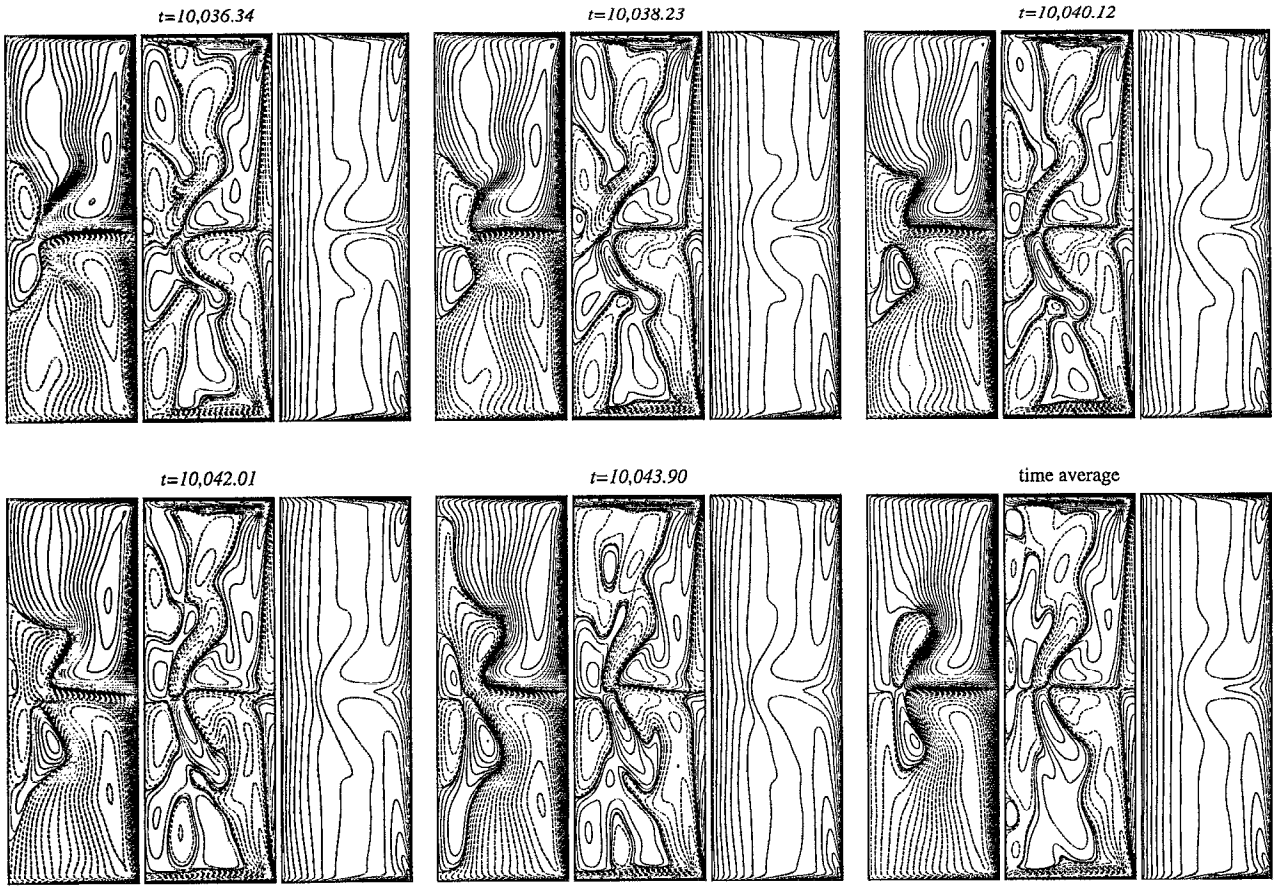

FIG. 15. (*Continued.*)

has only been observed from the periodic branch and for Re≥3020. This is consistent with the conclusion of Valentine and Jahnke[9] that for Re≤3000, the Z_2 symmetry is robust. However, the Z_2 symmetry breaking observed on the 61×91 uniform grid for Re≥3020 appears to be due to insufficient grid resolution. If the same asymmetric initial conditions are used in a calculation on the 101×151 stretched grid, the flow eventually, after about 1000 units, evolves to the same Z_2-symmetric periodic flow as that found when Z_2 symmetry was imposed. This resymmetrization of the flow is illustrated in Fig. 12 for Re=3500. For the first 100 or so time units of the evolution, the flow is very non-Z_2 symmetric. However, by $t=500$, it has settled down to an almost Z_2 symmetric flow; the small perturbations away from Z_2 symmetry are gradually damped, but are still discernible at $t=1250$, particularly in the η contours about the midplane. By $t=2025$, as illustrated in Fig. 13, the flow has settled onto the Z_2-symmetric, $T\approx 28$ periodic branch found when Z_2 symmetry was imposed. Figure 13 shows the flow over one period of this oscillation, together with its time average. The figure should be compared with Fig. 11, showing the $T\approx 28$ periodic flow for the same Re and H/R when Z_2 symmetry is imposed; the two flows are the same. This would suggest that the Z_2 symmetry is very robust. However, the situation is not entirely resolved. A similar calculation at Re=3200 does not resymmetrize on the 101×151 stretched grid, but instead evolves to a modulated, $T\approx 18.9$, non-Z_2-symmetry flow (the time series for this flow is shown in Fig. 14 along with contours of the flow over approximately 18.9 time units in Fig. 15, showing the "flip–flopping" of the high Γ radial jet across the midplane), similar to that found on the 61×91 grid. Whereas a calculation started impulsively from rest at the same parameter values without the Z_2 symmetry imposed evolves to the $T\approx 28$ periodic Z_2-symmetric flow found when the symmetry is imposed. This all suggests that the Z_2-symmetry flows are stable for Re≤3500, but that there also exist non-Z_2-symmetric flows in that parameter range. However, it is not clear whether the observed non-Z_2-symmetric flows are present due to insufficient grid resolution, or if the non-Z_2-symmetric flow branch is actually disjoint from the Z_2-symmetric branches and we are able to reach it via "nonstandard" initial conditions. In order to determine this, one would need to double the grid points to 201×601 and then probably to 401×1201, with a corresponding halving of δt to 0.0001 and 0.000 05, until consistent dynamical behavior is achieved on two consecutive doublings of the resolution, and compute several cases at various Re with a variety of initial conditions. Such a study, given the long evolution times required (about 10 000 time units) is simply beyond the computational resources presently available to the author.

[1] J. M. Lopez, "Axisymmetric vortex breakdown. Part 1. Confined swirling flow," J. Fluid Mech. **221**, 533 (1990).

[2]G. L. Brown and J. M. Lopez, "Axisymmetric vortex breakdown. Part 2. Physical mechanisms," J. Fluid Mech. **221**, 553 (1990).
[3]J. M. Lopez and A. D. Perry, "Axisymmetric vortex breakdown. Part 3. Onset of periodic flow and chaotic advection," J. Fluid Mech. **234**, 449 (1992).
[4]A. Spohn, "Ecoulement et éclatement tourbillonnaires engendrés par un disque tournant dans une enceinte cylindrique," Thèse de Doctorat d'Université, Université Joseph Fourier Grenoble I, March 1991.
[5]A. Spohn, M. Mory, and E. J. Hopfinger, "Observations of vortex breakdown in an open cylindrical container with a rotating bottom," Exp. Fluids **14**, 70 (1993).
[6]J. M. Hyun, "Flow in an open tank with a free surface driven by the spinning bottom," J. Fluid Eng. **107**, 495 (1985).
[7]O. Daube, "Numerical simulations of axisymmetric vortex breakdown in a closed cylinder," Lectures Appl. Math. **28**, 131 (1991).
[8]M. P. Escudier, "Observations of the flow produced in a cylindrical container by a rotating endwall," Exps. Fluids **2**, 189 (1984).
[9]D. T. Valentine and C. C. Jahnke, "Flows induced in a cylinder with both end walls rotating," Phys. Fluids **6**, 2702 (1994).
[10]S. L. Bragg and W. R. Hawthorne, "Some exact solutions of the flow through annular cascade actuator discs," J. Aeronaut. Sci. **17**, 243 (1950).
[11]P. A. Davidson, "The interaction between swirling and recirculating velocity components in unsteady, inviscid flow," J. Fluid Mech. **252**, 357 (1989).
[12]A. Arakawa, "Computational design for long-term numerical integration of the equations of fluid motion: Two-dimensional incompressible flow. Part 1," J. Comput. Phys. **1**, 119 (1966).
[13]M. J. Miller and R. P. Pearce "A three-dimensional primitive equation model cumulonimbus convection," Q. J. R. Meteorol. Soc. **100**, 133 (1974).
[14]G. P. Williams, "Thermal convection in a rotating fluid annulus: Part 1. The basic axisymmetric flow," J. Atmos. Sci. **24**, 144 (1967).
[15]M. D. Impey, D. S. Riley, A. A. Wheeler, and K. H. Winters, "Bifurcation analysis of solutal convection during directional solidification," Phys. Fluids A **3**, 535 (1991).
[16]S. J. Tavener, "Stability of the $O(2)$-symmetric flow past a sphere in a pipe," Phys. Fluids **6**, 3884 (1994).
[17]P. Constantin, C. Foias, and R. Temam, "On the large time Galerkin approximation of the Navier–Stokes equations," SIAM J. Num. Anal. **21**, 615 (1984).
[18]J. Serrin, "On the stability of viscous fluid motion," Arch. Rat. Mech. Anal. **3**, 1 (1959).